

Making a Superior Oxide Corrosion Passivation Layer on Aluminum Using Ozone

A. Kuznetsova and J. T. Yates, Jr.*

Surface Science Center, Department of Chemistry, University of Pittsburgh,
Pittsburgh, Pennsylvania 15260

G. Zhou and J. C. Yang

Materials Science & Engineering Department, University of Pittsburgh,
Pittsburgh, Pennsylvania 15261

Xidong Chen

Materials Science Division, Argonne National Laboratory, Argonne, Illinois 60439

Received September 11, 2000. In Final Form: January 16, 2001

Aluminum oxidation by ozone produces an aluminum oxide layer which is superior in its corrosion properties compared to natural oxide, as measured by electrochemical methods. The electrochemically measured impedance of the O₃-grown films is ~10 times greater than that of O₂-grown films of equivalent thickness. An enhanced pitting potential is observed for the O₃-grown oxide film. Transmission electron microscopy results show that the pore size of O₃-grown oxide films is considerably smaller than that of O₂-grown films. Transmission electron microscopy electron diffraction studies show that the amorphous O₃-grown films are ~4% more dense than the O₂-grown film. The initial sticking coefficient for ozone on atomically clean polycrystalline aluminum is 3.8 times larger than for oxygen at 300 K.

1. Introduction

In this paper, we report using ozone, O₃, to produce a passivating film of aluminum oxide on polycrystalline aluminum surfaces. The work continues our previous investigations, where the oxidation of the Al(111) single-crystal surface and also polycrystalline Al surfaces was performed using energetic oxidizing species to produce enhanced corrosion passivating oxide layers on Al. The oxide films produced by these methods were studied by surface science techniques (Auger electron spectroscopy (AES), X-ray photoelectron spectroscopy (XPS), high-resolution electron energy loss spectroscopy (HREELS), electrochemical impedance spectroscopy (EIS), and transmission electron microscopy (TEM)^{1–4}).

The strong oxidizing ability of ozone enables the surface of metals and semiconductors to form a superior corrosion passivation film. Thus, the oxidation of porous silicon by O₃ produces a passive SiO₂ layer thereby preventing microelectronic devices from degradation.⁵

Passivation techniques using highly concentrated ozone have previously been applied to steel tubing used for corrosive gases. The ozone formed an anticorrosive passivation film with a thickness up to 60 Å, which showed excellent corrosion-protection properties.⁶

The treatment of chemical vapor deposition (CVD)-created tantalum oxide films with ozone was reported

recently. Ozone produces an oxide with lower leakage current in these films, and this is attributed to the reduction of the concentration of impurity of carbon and hydrogen as well as to the removal of oxygen vacancies.⁷

In this paper we study the aluminum oxide film produced by ozone on polycrystalline aluminum surfaces and compare its corrosion and structural properties to oxide layers formed from oxygen alone.

II. Experimental Section

A. Vacuum Techniques. The experiments were done under ultrahigh vacuum (UHV) conditions at a base pressure of 2×10^{-10} Torr. The chamber is equipped with a 360 L/s ion pump, a 150 L/s turbo pump, and a titanium sublimation pump. A quadrupole mass spectrometer (UTI Instruments/100 C) was used for residual gas analysis.

A Perkin-Elmer Auger spectrometer (model 11-010 cylindrical mirror analyzer) was used for the characterization of Al samples by AES. The primary electron beam energy used was 3 keV, and an emission current of 0.5 μA was employed.

B. Preparation of Al Samples. The samples of polycrystalline Al (99.999%, Goodfellow) were prepared as reported previously.³ They were mechanically polished (600 grit) using a Buehler Minimet polisher and then electropolished in a 1% NaOH solution. Then the Al samples were transferred to the vacuum chamber and cleaned with Ar⁺ bombardment ($E_{Ar^+} = 1$ keV, $I/A \sim 8$ μA/cm²). The purity of the Al sample surface was monitored by AES. The absence of measurable O(KLL) intensity shows that the Al sample surface contains less than 1 atom % of oxygen in the depth of Auger sampling. No other impurities could be detected by AES.

C. Ozone Production and Dosing. Ozone was prepared using an ozone generator described previously.⁸ Oxygen (99.994%

(1) Ebinger, H. D.; Yates, J. T., Jr. *Surf. Sci.* **1998**, *413*, 1.

(2) Ebinger, H. D.; Yates, J. T., Jr. *Phys. Rev. B* **1998**, *57*, 1976.

(3) Kuznetsova, A.; Burleigh, T. D.; Zhukov, V.; Yates, J. T., Jr. *Langmuir* **1998**, *14*, 2502.

(4) Popova, I.; Zhukov, V.; Yates, J. T., Jr. *Appl. Phys. Lett.* **1999**, *75*, 3108.

(5) Frotscher, U.; Rossow, U.; Ebert, M.; Pietryga, C.; Richter, W.; Berger, M. G.; ArensFischer, R.; Munder, H. *Thin Solid Films* **1996**, *276*, 36.

(6) Koike, K.; Inoue, G.; Takata, T.; Fukuda, T. *Jpn. J. Appl. Phys., Part 1* **1997**, *36*, 7437.

(7) Moon, B. K.; Isobe, C.; Aoyama, J. *J. Appl. Phys.* **1999**, *85*, 1731.

(8) Yates, J. T., Jr. *Experimental Innovations in Surface Science*; Springer Verlag: New York, 1998; p 702. Zhukov, V.; Popova, I.; Yates, J. T., Jr. *J. Vac. Sci. Technol., A* **2000**, *8*, 992.

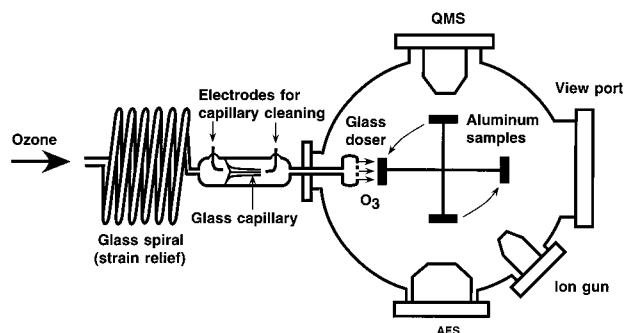


Figure 1. Ultrahigh vacuum apparatus for aluminum oxidation by oxygen and ozone.

pure, VWSCO) was used for ozone synthesis. After flowing oxygen at 1 atm through the high-voltage capacitor in an all-glass vacuum system, the mixture of produced ozone and unreacted O_2 was passed through a silica gel trap cooled by an acetone/dry ice bath at 195 K. Oxygen was pumped from the silica gel at 195 K, and then O_3 was liberated by gentle heating. The purity of the effluent gas from the generator was checked by measuring the pressure change during decomposition⁸ and the O_3 was found to be 97% pure (3% O_2).

The ozone generator was connected using a strain-free design to a glass doser inside the UHV chamber using a glass spiral, as shown in Figure 1. The glass doser consists of a cylindrically shaped head containing multiple holes for uniform O_3 deposition on the sample. The doser assembly also contains a glass capillary of ~ 0.06 mm inner diameter to control the conductance of O_3 into the UHV chamber. The dosing was calibrated with O_2 gas and was shown to give an absolute delivery rate of 2.9×10^{14} molecules·Torr⁻¹·s⁻¹. From the calculation of the fractional interception of the gas beam by the sample, estimated to be $\alpha = 0.6$ from the doser/sample geometry,⁹ and by taking into account the difference in molecular weights of O_2 and O_3 , the incident flux of O_3 and O_2 is respectively 2.7×10^{13} O_3 molecules·cm⁻²·s⁻¹·[P (Torr)] and 3.4×10^{13} O_2 molecules·cm⁻²·s⁻¹·[P (Torr)], where P (Torr) is the pressure in the high-pressure gas storage line (both O_3 and O_2 were used at ~ 4 Torr).

The atomically clean Al samples were oxidized with O_3 supplied through the doser directly to the sample surface. The background pressure in the UHV chamber during the O_3 exposure increases to 10^{-8} Torr.

For comparison the oxidation of clean aluminum surfaces was also carried out using molecular oxygen.

D. Electrochemical Impedance Measurements and Tafel Analysis of Al_2O_3/Al Films. After the Al samples were oxidized with O_3 or O_2 , they were removed from the UHV chamber and placed in an electrochemical cell for EIS measurements. The electrochemical cell was described previously.³ It contains a counter electrode (Pt), a reference electrode (saturated calomel, SCE) and a working electrode (Al sample). The solution of 3.5% NaCl was deaerated (N_2 , 99.998% gas bubbling) for 30 min before the measurements. The impedance spectra were measured at open circuit potential.

Electrochemical impedance spectra were taken with a potentiostat-galvanostat programmable generator electrochemical impedance apparatus (model PGZ301 radiometer). The frequency applied ranges from 100 kHz to 10^{-2} Hz. The amplitude of the applied ac potential was 5 mV root mean square. The data acquisition was carried out with Voltalab 40 software.

Linear polarization measurements (Tafel analysis) were performed in the same electrochemical cell as EIS measurements. The scan rate used was 0.8 mV/s. The range of potential applied was -1.40 to -0.66 V. The data analysis was performed using Voltalab 40 software.

E. Transmission Electron Microscopy Analysis. The structure of the amorphous Al_2O_3 film was examined by TEM. To prepare the TEM specimen, the ~ 20 Å oxide was scraped off the Al substrate with a razor blade and dispersed in propanol using an ultrasonic agitator. The propanol and oxide suspension

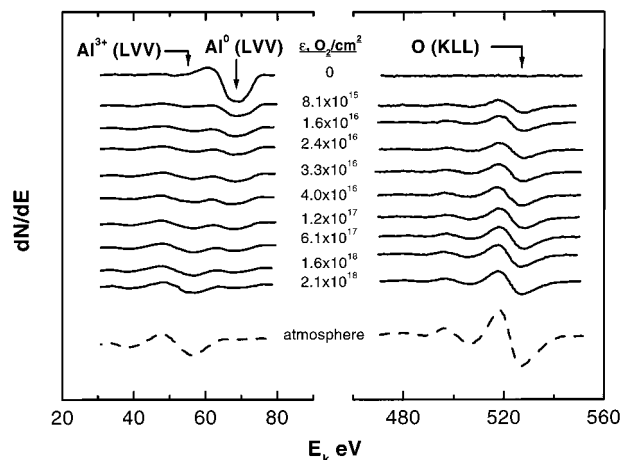


Figure 2. Auger spectra of aluminum oxidized by O_2 at 300 K.

was placed on a lacey carbon grid and air-dried. A JEOL200CX TEM, operated at 200 keV, was utilized to examine the pore structure of the alumina. Energy-dispersive X-ray (EDX) spectroscopy was performed on a JEOL2000FX TEM equipped with a Phillips EDX detector, to determine that the examined area is alumina and not the carbon film. High-resolution electron microscopy (HREM) studies were performed in a Phillips CM-200FEG microscope equipped with a Gatan Image Filter (GIF), which has a spatial resolution of 1.8 Å. The same TEM was used to digitally capture the selected area electron diffraction pattern (SAED).

A radial distribution function (RDF) is often used to describe amorphous structures.¹⁰ This function, $J(r)$, is defined as the number of atoms lying at distances between r and $r + dr$ from the center of an arbitrary atom. We can write this function as

$$J(r) = 4\pi r^2 \rho(r) \quad (1)$$

where $\rho(r)$ is a two-body correlation function. This function, $\rho(r)$, is equal to the average density, ρ^0 , at very large values of r where the distribution of atoms appears homogeneous from the center. Hence, we can measure the average density of the aluminum oxide film from the radial distribution function.

The radial distribution function is extracted from the digitally captured SAED pattern of the amorphous alumina. The microscope was calibrated by using a standard aluminum specimen. Inelastic scattering intensity was automatically excluded by the energy-filter camera, with which all diffraction patterns were digitally recorded. Small-angle scattering was also cut off before Fourier transformation in order to remove the strong dynamic effect of electron diffraction. This cutoff should not affect our results because small-angle scattering does not contribute to the term, which would yield the radial distribution function. An edge smooth function was applied when the Fourier transform was performed. This procedure was used to avoid artificial oscillations in the resulting radial distribution function.

III. Results

A. Auger Spectroscopy Study of Aluminum Oxidation at 300 K. Auger spectra of the aluminum surface oxidized with $O_2(g)$ at 300 K are shown in Figure 2. The growth of the Al^{3+} (LVV) peak at 56 eV and the O(KLL) feature at 525 eV and the decrease of the Al^0 (LVV) (68 eV) peak are observed with increasing O_2 exposure. At the final level for oxidation (maximum exposure up to $\epsilon(O_2) = 2.1 \times 10^{18}$ O_2/cm^2) the Al^0 peak may still be faintly observed in the spectrum. The bottom spectrum in Figure 2 was measured after the sample was exposed to atmosphere and will be discussed later.

(10) Elliott, S. R. *Physics of Amorphous Materials*; Wiley: New York, 1990.

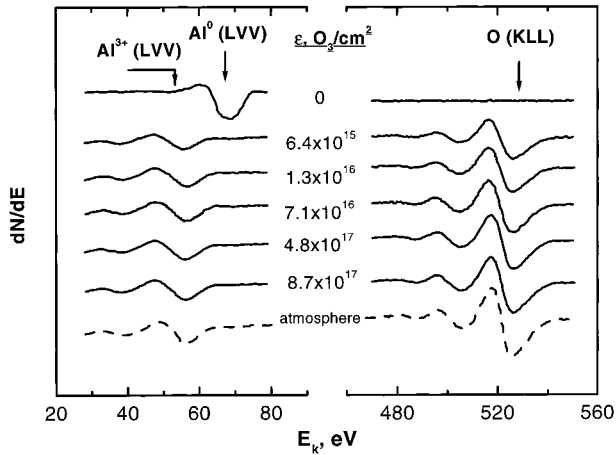


Figure 3. Auger spectra of aluminum oxidized by O_3 at 300 K.

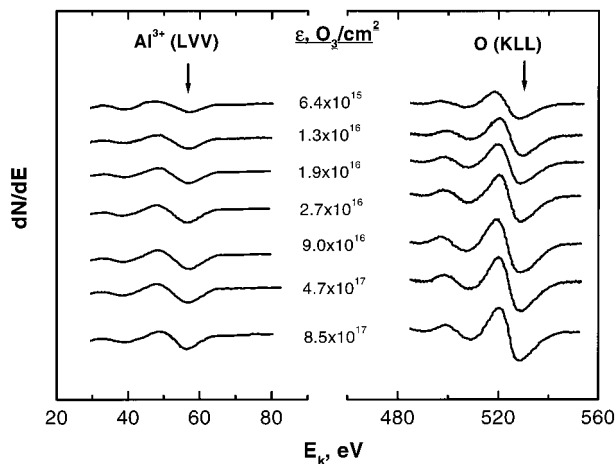


Figure 4. Auger spectra of aluminum oxidized by $O_2 + O_3$ at 300 K.

Figure 3 shows the growth of Al^{3+} and O^{2-} Auger features when the aluminum surface is oxidized with ozone. Comparison of the Auger spectral development in Figures 2 and 3 shows that O_3 more rapidly oxidizes Al than does O_2 for equivalent exposures. By an exposure of $6.4 \times 10^{15} O_3/cm^2$ the Al^0 peak completely disappears. The saturation level for the oxidation process occurs at an exposure of $\epsilon(O_3) = 7 \times 10^{16} O_3/cm^2$.

Figure 4 shows the Auger spectra of aluminum oxidized with oxygen ($\epsilon(O_2) = 2.1 \times 10^{18} O_2/cm^2$) followed by the oxidation by ozone. The addition of $6.4 \times 10^{15} O_3/cm^2$ causes the disappearance of the small Al^0 peak, similar to the oxidation by ozone in the previous experiment (Figure 3). The saturation intensity of the oxygen signal for the Al + $O_2 + O_3$ sequence is the same as for the Al + O_3 reaction, as shown in Figure 5. The peak-to-peak intensity of the oxygen peak of the oxide film grown by O_3 is 2.4 times larger than that of the O_2 -grown film, both produced under saturation coverage.

The initial sticking coefficient for ozone adsorption evaluated by the initial slope of the oxygen signal in the Auger spectra is shown in the insert to Figure 5. The initial sticking coefficient of ozone is 3.8 times higher than that of oxygen.

Figures 2 and 3 show also the change in the Auger peaks when the samples were exposed to atmosphere. To calibrate the Auger spectrometer after each exposure of the chamber to atmosphere, the spectrometer sensitivity

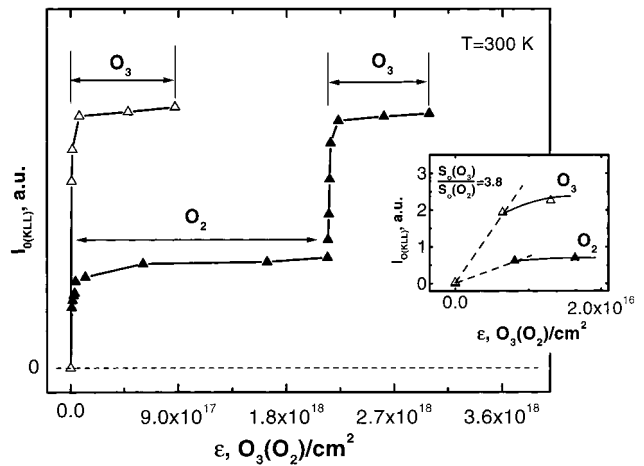


Figure 5. Kinetics of aluminum oxidation by O_2 and O_3 measured by Auger spectroscopy.

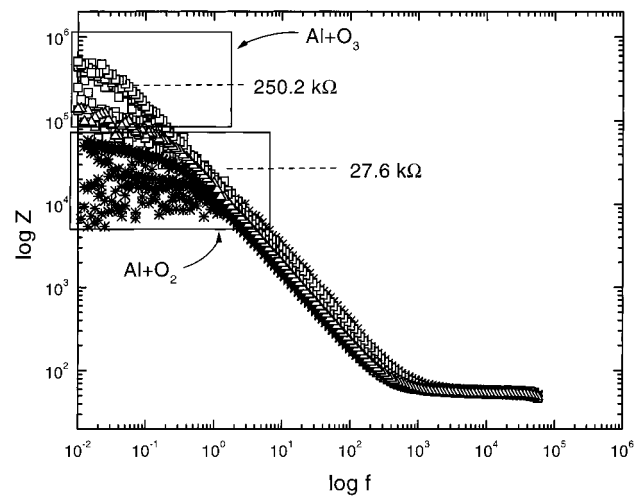


Figure 6. EIS of aluminum oxidized with O_2 and O_3 , showing results for 16 measurements.

was calibrated using a Au sample measuring the Au(MNN) transition peak at 69 eV. The intensity of the Au Auger peak after exposure to the atmosphere was identical to that found under vacuum, showing that the intensity increase for O is not due to a gain change in the spectrometer.

A small additional growth of the oxygen Auger peak-to-peak intensity peaks both for ozone-formed and for oxygen-formed oxides is observed upon atmospheric exposure. The oxygen signal from the sample oxidized with ozone is 80% of the saturation level compared to that after atmospheric exposure. The Auger measurements also showed the oxygen signal from oxygen-formed oxides is about 83% of the signal for the ozone-formed oxide after both oxide films were exposed to the atmosphere.

B. Electrochemical Impedance Spectroscopy Study of the Various Oxide Films. Figure 6 shows the EIS spectra for 16 experiments where aluminum was oxidized with ozone and with oxygen using the same exposure of $2.0 \times 10^{18} O_3/cm^2$ or O_2/cm^2 . One sample (shown as triangles) is oxidized by oxygen (up to an exposure of $2.0 \times 10^{18} O_2/cm^2$) followed by additional oxidation by ozone up to an exposure of $3.0 \times 10^{19} O_3/cm^2$. This treatment raises the film impedance, Z , into the high range observed for samples oxidized with pure O_3 .

The values of resistance and capacitances were evaluated¹¹ by fitting the formula

Table 1. Electrochemical Properties for Ozone- and Oxygen-Formed Oxides

sample no.	capacitance, μF	resistance, $\text{k}\Omega$	film thickness, \AA
Ozone-Grown Oxide			
1	6.0	118.7	14.2
2	6.0	83.3	14.2
3	6.0	70.0	14.2
4	4.6	81.3	18.5
5	5.1	449.4	16.7
6	4.5	151.1	18.9
7	6.0	345.4	14.2
8	6.0	450.2	14.2
9	6.0	502.4	14.2
av	5.6 ± 0.6	250.2 ± 165.9	15.1 ± 1.6
Oxygen-Grown Oxide			
1	5.3	11.0	16.0
2	4.0	18.7	21.3
3	5.1	28.8	16.7
4	4.8	14.1	17.7
5	6.0	37.7	14.2
6	6.0	40.2	14.2
7	6.0	42.7	14.2
av	5.3 ± 0.6	27.6 ± 11.1	16.0 ± 1.8
Oxygen + Ozone Grown Oxide			
1	6.0	98.0	14.2

$$Z = R_s + R_o / (1 + \omega R_o C)^2 + j(-\omega R_o^2 C) / [1 + (\omega R_o C)^2] \quad (2)$$

where Z is the total impedance, in ohms; R_s and R_o are the resistances of the electrolyte solution and the oxide films, respectively, in ohms; C is the capacitance of oxide, in farads; $\omega = 2\pi f$, where f is the ac voltage frequency, in Hz; and $j = -1^{1/2}$.

The resistance and capacitance values are shown in Table 1. The average resistances for the oxide films grown by O_2 exposure and by O_3 exposure are marked as dashed lines in Figure 6. The average resistance of the ozone-grown layer is ~ 10 times higher than that for the oxygen-grown layer. The similarity in capacitance values (as judged by the slopes of the curves in the intermediate frequency region) implies a similar thickness for the two oxide films with the assumption of a similar dielectric constant for the oxide film in each case. The thickness of the oxide was calculated using the formula for a parallel plate capacitor

$$C = \epsilon \epsilon_0 A / d \quad (3)$$

where C is the capacitance, in farads; ϵ is the dielectric constant; $\epsilon_0 = 8.85 \times 10^{-12} \text{ F/m}$; A is the area of the sample, m^2 ; and d is the thickness of the oxide, in meters. With a dielectric constant of 8.5, the calculated average thickness for the ozone-grown oxide is 15.1 \AA and for the oxygen-grown oxide the average thickness is 16.0 \AA . The thickness for the $\text{O}_2 + \text{O}_3$ grown oxide is 14.2 \AA . Considering the errors in this experiment, all three oxide films exhibit a similar average film thickness as measured by the capacitance method, $\sim 15 \text{ \AA}$. The value of this film thickness as measured electrochemically may differ from its true thickness as a result of the assumption of a dielectric constant in eq 3.

The sample oxidized with oxygen followed by oxidation with ozone shows higher resistance than that obtained for oxygen-grown oxide alone, with an impedance in the lower range found for ozone-oxidized samples.

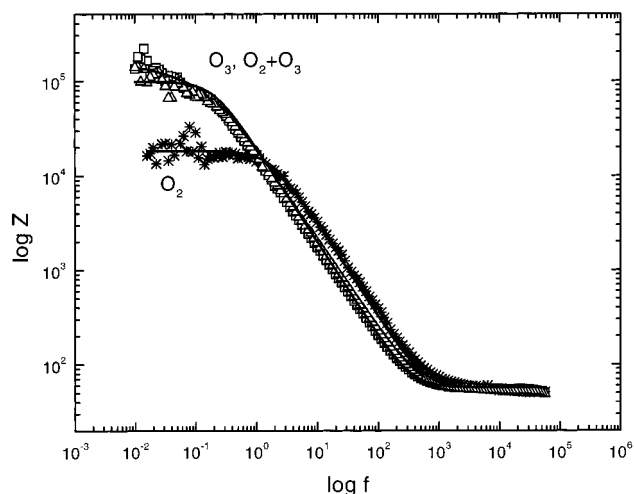
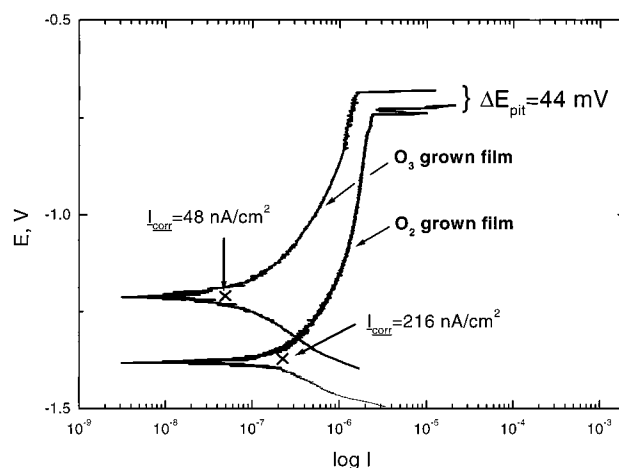
**Figure 7.** Representative EIS plots of aluminum oxidized with O_2 , O_3 , and $\text{O}_2 + \text{O}_3$.**Figure 8.** Tafel plots for O_2 - and O_3 -oxidized samples.

Figure 7 shows representative plots for ozone and oxygen oxidized samples and fitting curves corresponding to formula 1. The third sample (marked as triangles) was oxidized by oxygen (O_2 exposure = $2.0 \times 10^{18} \text{ O}_2/\text{cm}^2$) followed by oxidation with ozone up to an exposure of $3.0 \times 10^{19} \text{ O}_3/\text{cm}^2$.

C. Tafel Measurements. The linear polarization measurements present an independent measurement of the corrosion properties of the aluminum oxide layers formed by oxygen or ozone. Figure 8 shows representative Tafel plots measured for two oxide films. The ozone-formed oxide shows a corrosion current density of 48 nA/cm^2 ; the oxygen-formed oxide shows a corrosion current density of 216 nA/cm^2 . The E_{pit} (pitting potential) values for the ozone-formed oxide is higher by 44 mV , showing superior oxide film stability toward pitting. Thus the impedance measurements (Figures 6 and 7) and the corrosion current density and pitting potential measurements (Figure 8) clearly show together that the ozone-grown oxide film is superior to the oxygen grown oxide film at equivalent gas exposures after exposure to the atmosphere.

D. TEM Measurements. Figure 9a is a bright field image from the specimen oxidized with oxygen, which shows that the oxide film contains many pores. The size of these pores is not uniform, ranging from 30 to 700 \AA , where the typical pore diameter is 200 \AA . The SAED pattern taken from this area is shown in the upper-right inset of this figure. The diffuse ring pattern demonstrates that the oxide film is amorphous. Figure 9b shows the

(11) Tait, W. S. *An Introduction to Electrochemical Corrosion Testing for Practicing Engineers and Scientists*; PairODocs Publications: Racine, WI, 1994; p 109.

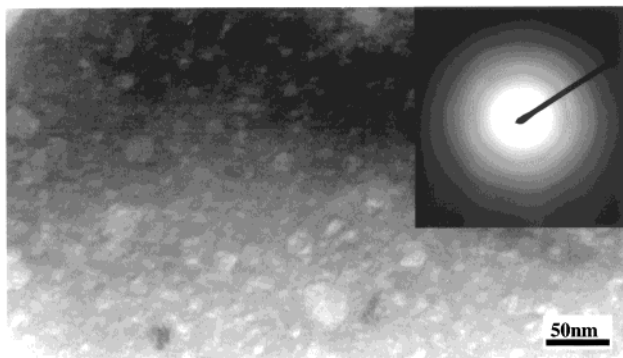
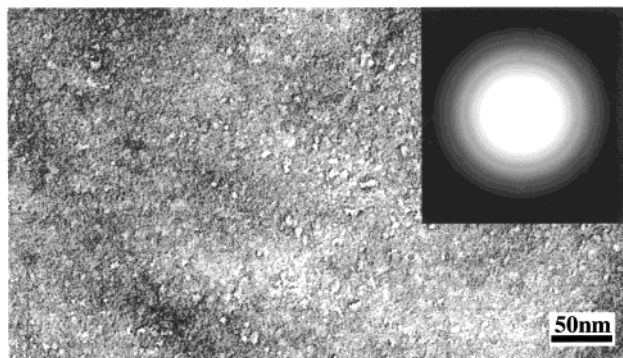
a) O₂-oxidized Al**b) O₃-oxidized Al**

Figure 9. TEM images for O₂- and O₃-oxidized samples: (a) O₂-oxidized sample; (b) O₃-oxidized sample.

bright field image of the ozone-produced specimen, where the inset is the SAED pattern corresponding to this area. There are also many pores in the ozone-produced film. Their diameter ranges from a few angstroms to 100 Å with an average diameter of 40 Å, which is much smaller than that observed for the oxygen-produced film. The SAED pattern reveals its amorphous structure. The compositions of the two oxide films were determined by EDS in order to show that the examined area contained aluminum.

High-resolution electron microscopy imaging was employed to investigate the microstructures of the oxides at atomic scale. The HREM images in Figure 10 show the representative microstructural characteristics of the two specimens. Figure 10a corresponds to the oxygen-produced film, which shows that the pores have circular shape with a diameter of 200 Å. The image in Figure 10b corresponds to the ozone-produced film, where the diameter of this typical pore is about 10 Å.

Figure 11 shows the radial distribution function of the oxygen-produced and ozone-produced Al samples. Above $r = 0.6$ nm, the ozone-produced film has a higher $J(r)$ value than the oxygen-produced specimen which corresponds to ~4% higher density of the alumina produced by ozone.

IV. Discussion

A. Initial Kinetics of Oxidation by O₃ Compared to O₂. The initial sticking coefficient for adsorption of O₃ at 300 K on polycrystalline Al is 3.8 times greater than for O₂ adsorption as seen in Figure 5. A qualitatively similar ratio $S_0(\text{O}_3)/S_0(\text{O}_2)$ has been observed for adsorption on Al(111), where a factor of 6.7 was measured.¹² For the oxidation of Pt(111) the ratio of $S_0(\text{O}_3)/S_0(\text{O}_2)$ was 4.8.¹³

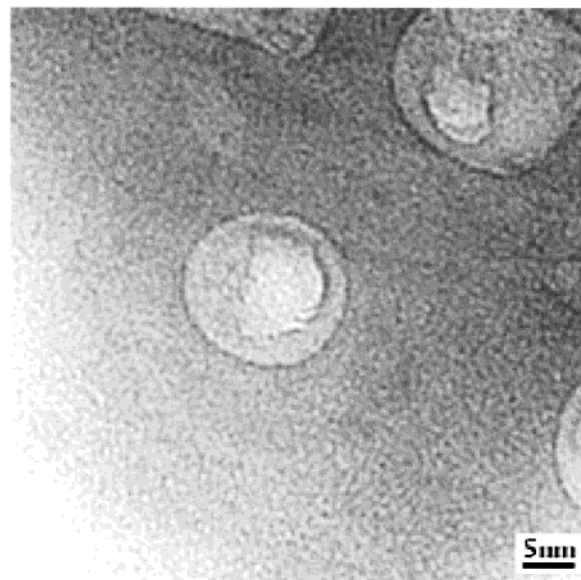
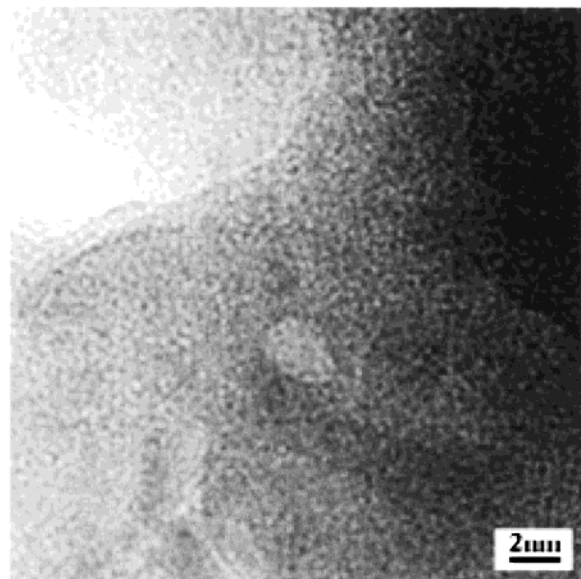
a) O₂-oxidized Al**b) O₃-oxidized Al**

Figure 10. HREM images for O₂- and O₃-oxidized samples: (a) O₂-oxidized sample; (b) O₃-oxidized sample.

A saturation effect for O₃ adsorption is observed to occur for exposures above $\sim 1.3 \times 10^{16}$ O₃/cm² where the rate of adsorption decreases to almost zero as seen in Figure 5.

These results clearly show that the initial surface reactivity of O₃ both with polycrystalline Al and with Al(111) exceeds that of O₂ by a large factor.

B. TEM Studies of Oxide Film Morphology and Density. Figures 9 and 10 show a transmission electron micrograph comparison between Al₂O₃ films grown with O₃ and with O₂. The average size of the pores observed in the O₃-grown film is 40 Å, whereas for the O₂-grown film the average pore size is 200 Å.

(12) Zhukov, V.; Popova, I.; Yates, J. T., Jr. *Langmuir*, submitted.
 (13) Saliba, N. A.; Tsai, Y.-L.; Koel, B. E. *J. Phys. Chem. B* **1999**, *103*, 1532.

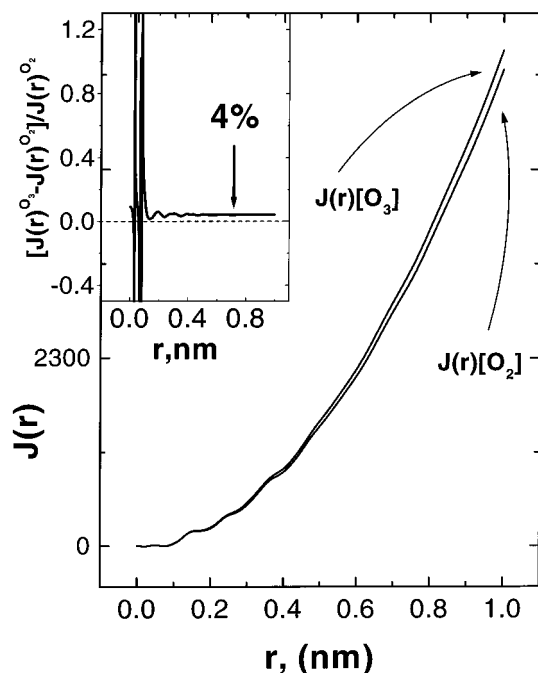
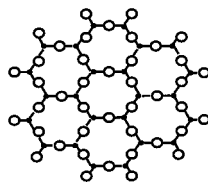


Figure 11. Radial distribution function for O_2 - and O_3 -oxidized samples, $J(r)$. The relative difference in $J(r)$ functions for O_2 - and O_3 -oxidized samples, representing the difference in densities of 4% at large r , is shown in an insert in the left top corner.

I. Ideal Al_2O_3



II. Strained Defective Oxide

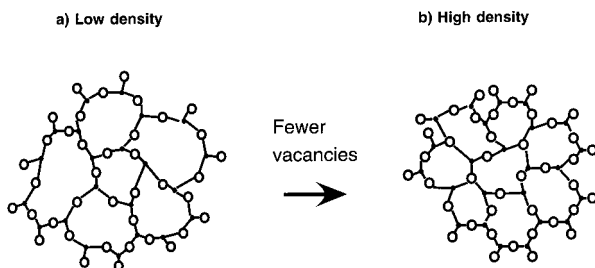


Figure 12. Schematic 2D representation of aluminum oxide structures.

By using electron diffraction measurements (Figure 11) for the amorphous Al_2O_3 films, we have found that the O_3 -produced oxide film has a density which is 4% greater than that observed for the O_2 -produced oxide films.

This result may be understood from the viewpoint of the work of Felhner and Mott,¹⁴ in which a thin oxide film on aluminum surfaces may be considered to be strained as schematically shown in Figure 12. The strained film will have large pores due to the abundance of oxygen vacancies. Such an effect will result in a lower density of the Al_2O_3 film than for "ideal" stoichiometric Al_2O_3 as

observed in comparing the radial distribution function for the O_2 -grown Al_2O_3 and the O_3 -grown Al_2O_3 in Figure 11. O_3 is able to reduce the density of oxygen vacancies causing the pore size to decrease and the film density to increase. The differences in oxide film structure implied by Figure 12 at the atomic size level is probably connected to the differences in pore size shown in Figures 10 and 11 at the 10–100 Å level of measurement.

C. Corrosion Protection by Capacitor-like Layer.

Figure 6 and Table 1 show that the electrochemical impedance spectroscopy measurement for O_3 -produced oxide films are superior by about a factor of 10 in their impedance to O_2 -produced films.

The thickness of the oxide films studied is identical (~ 14 – 16 Å) after they are transferred in air to the electrochemical apparatus, based on the slopes of the EIS plots in the intermediate frequency region and the assumption of a film dielectric constant of 8.5 in all cases. The thickness of the oxide films after they are exposed to atmosphere exceeds that measured by AES after oxidation in the vacuum system. This is due to additional atmospheric oxidation of the thin film. The increased impedance measured for the O_3 -grown films, therefore, does not depend on the production of the thicker oxide film by exposure to air. Instead it represents a significant physical difference between O_3 -grown and O_2 -grown oxide films, even after massive exposure to air.

In analogy to these findings, the existence of a high impedance transition layer was detected on O_3 -oxidized silicon and germanium surfaces as well by the capacitance and current–voltage measurements.^{15,16}

The study of the silicon oxidation by ozone showed that the displacement of interfacial Si atoms is much smaller than for oxygen oxidation¹⁶ in SiO_2/Si samples. Ozone is postulated to produce a more homogeneous SiO_2 film than O_2 . In addition, acid etching of the SiO_2 film grown by O_3 gives the constant rate of oxide layer depletion, also showing good homogeneity of the oxide when it has been produced from ozone. Measurements of impedance of ozone-formed silicon dioxide showed a 3-fold increase compared to native oxide. Interestingly, the total thickness of the O_3 -grown oxide is similar to the thermally grown oxide suggesting also that a structural change is responsible for enhanced passivation of the Si to corrosion.

Oxidation of Ge by ozone resulted in oxide films which are closely similar to dense stoichiometric GeO_2 ,¹⁵ which possesses excellent electrical characteristics.

The intrinsic properties of aluminum oxide films grown from O_3 differ from O_2 -grown films in three respects as measured here: (1) The O_3 -grown films have a $\sim 4\%$ higher density. (2) The O_3 grown films exhibit smaller pore sizes. (3) The O_3 -grown films exhibit a 10-fold higher electrical impedance as well as improved electrochemical corrosion behavior, as measured by the Tafel analysis. The pitting potential differences may also indicate an enhancement of corrosion passivation by O_3 oxidation compared to O_2 oxidation.

Surprisingly, the aluminum preoxidized with oxygen with subsequent oxidation by ozone also showed superior corrosion passivation properties, as shown in Figures 6 and 7. Apparently, the high activity of ozone toward metals is caused by the diffusion of reactive species through the porous films "sealing" vacancies, such as these shown

(15) Cracium, C. V.; Boyd, I. W.; Hutton, B.; Williams, D. *Appl. Phys. Lett.* **1999**, *75*, 1261.

(16) Kurokawa, A.; Nakamura, K.; Ichimura, S. *Appl. Phys. Lett.* **2000**, *76*, 493.

(14) Felhner, F. P.; Mott, N. F. *Oxid. Met.* **1970**, *2*, 59.

schematically in Figure 12. A similar phenomenon was observed on a semiconductor/insulator ($\text{Ta}_2\text{O}_5/\text{Si}$) film which was annealed with ozone. TEM images showed an increase in the oxide thickness not only for the top insulating layer but also of the native SiO_2 buried under the insulator.⁷

V. Conclusions

The following conclusions have been reached in this study:

1. O_3 produces oxide films on polycrystalline aluminum surfaces which are superior in electrochemical corrosion passivation properties as shown by EIS and Tafel measurements. The impedance of the O_3 -grown films is ~ 10 times greater than that of O_2 -grown films of equivalent thickness, and an enhanced pitting potential is observed for the O_3 -grown oxide film.

2. The enhancement of corrosion passivation properties by O_3 -produced oxide films is observed after massive exposure to the atmosphere, indicating that an inherent

superior behavior exists for Al_2O_3 passive layers produced by O_3 .

3. Transmission electron microscopy results show that the pore size of O_3 -grown oxide films is considerably smaller than that of O_2 -grown films.

4. TEM electron diffraction studies show that the amorphous O_3 -grown films are 4% more dense than the O_2 -grown films. This is interpreted to mean that ozone-based oxidation produces more highly coordinated oxide structures which are inherently more corrosion resistant.

5. The application of O_3 to an O_2 -grown aluminum oxide film results also in enhanced corrosion resistance properties, presumably due to the healing of O-vacancy defect sites by chemically energetic O_3 .

Acknowledgment. We acknowledge with gratitude the support of the Air Force Office of Scientific Research and the National Science Foundation. We thank Dr. T. Nuhfer for his assistance with the TEM.

LA001300X